NANO LETTERS

Letter

pubs.acs.org/NanoLett

Nanostructured Ultrafast Silicon-Tip Optical Field-Emitter Arrays

Michael E. Swanwick,[†] Phillip D. Keathley,[‡] Arya Fallahi,[§] Peter R. Krogen,[‡] Guillaume Laurent,[‡] Jeffrey Moses,[‡] Franz X. Kärtner,[‡,§,⊥] and Luis F. Velásquez-García*[,†]

[†]Microsystems Technology Laboratories and [‡]Department of Electrical Engineering and Computer Science and Research Laboratory of Electronics, Massachusetts Institute of Technology, 77 Massachusetts Avenue, Cambridge, Massachusetts 02139, United States

[§]Center for Free-Electron Laser Science, Deutsches Elektronen-Synchrotron, Notkestralse 85, 22607 Hamburg, Germany

[⊥]Department of Physics and The Hamburg Centre for Ultrafast Imaging, University of Hamburg, Luruper Chaussee 149, 22761 Hamburg, Germany

S *Supporting Information*

ABSTRACT: Femtosecond ultrabright electron sources with spatially structured emission are an enabling technology for free-electron lasers, compact coherent X-ray sources, electron diffractive imaging, and attosecond science. In this work, we report the design, modeling, fabrication, and experimental characterization of a novel ultrafast optical field emission cathode comprised of a large (>100 000 tips), dense (4.6 million tips·cm^{-2}), and highly uniform (<1 nm tip radius deviation) array of nanosharp high-aspect-ratio silicon columns. Such field emitters offer an attractive alternative to UV photocathodes while providing a direct means of structuring the emitted electron beam. Detailed measurements and simulations show pC electron bunches can be generated in the multiphoton and tunneling regime within a single optical cycle, enabling significant advances in electron diffractive imaging and coherent X-ray sources on a subfemtosecond time scale, not possible before. At high charge emission yields, a slow rollover in charge is explained as a combination of the onset of tunneling emission and the formation of a virtual cathode.

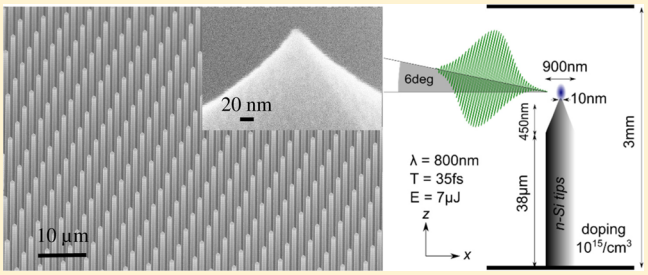

KEYWORDS: *Strong-field photoemission, ultrafast optics, field emission, nanosharp, silicon emitters, field emitter array*

Ultrafast-pulsed (<1 ps), ultrabright high-current electron sources are an enabling technology for such proposed ideas as table-top free-electron lasers, electron diffractive imaging,[1] and compact coherent X-ray generators.[2] State-of-the-art ultrafast cathodes are flat surfaces that use highly reactive materials to lower the work function and increase the quantum efficiency of single-photon absorption for ultraviolet (UV) pulses; these devices have short lifetimes and need to be fabricated and operated in ultrahigh vacuum.[3] Multiphoton and strong-field emission cathodes are an attractive alternative to circumvent these issues. Strong-field electron tunneling from solids without damage[4−9] occurs when the electric field of high-intensity optical pulses interacts with field enhancing structures to bend down the potential barrier at the surface such that the electron's tunneling time is shorter than one optical cycle,[10] with the potential for attosecond electron pulse generation.[11] Much of the previous work on nanostructured multiphoton and strong-field emission cathodes has focused on single metal tips that are serially manufactured;[12] in this work, we used wafer-level semiconductor batch fabrication techniques to create massively multiplexed arrays of nanosharp high-aspect-ratio single-crystal silicon pillars with high uniformity (>100 000 tips, 4.6 million tips·cm^{-2}, 4.4 nm average radius of curvature with a standard deviation of 0.6 nm), resulting in greatly enhanced array electron emission (Figure 1a). This also enables the generation of attosecond electron pulses at the tip surface with considerable charge, i.e., hundreds of fC from a single cycle near-IR drive source when used along with a THz source for charge extraction.[13,14] A high-aspect-ratio silicon column topped by a nanosharp tip achieves electron emission at low power by greatly enhancing the incident electric field; the massive multiplexing of the pillars with low tip radii spread drastically increases the total current emission and also structures the emission as a series of planar arrays of electron bunches. In a field emitter array, a broad tip radii distribution causes severe array subutilization because the emission current has an exponential dependence on the local surface electric field at the tips, and hence field factor of the emitters, which is inversely proportional to the tip radii. For ultrafast electron source applications achieving a homogeneous charge distribution[15] in the bunch is strongly desired, thereby making small variations in the tip dimensions essential. Here, we developed a fabrication process that attains small tip variation across the array as a result of the diffusion-limited oxidation step that sharpens the tips and we identified the current−voltage−optical

Received: April 29, 2014
Revised: July 18, 2014
Published: July 30, 2014

   dx.doi.org/10.1021/nl501589j | *Nano Lett.* 2014, 14, 5035−5043

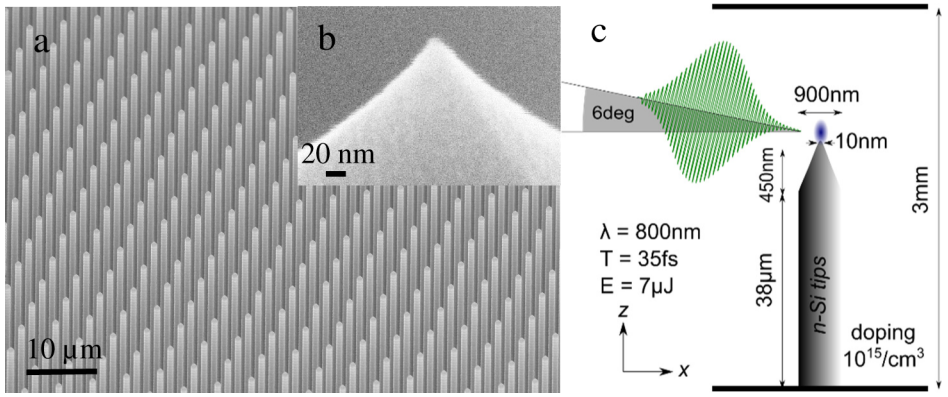

Figure 1. Images and schematic of emitter structure: (a) Scanning electron microscope (SEM) image of uniform array of high-aspect-ratio Si columns with 5 μm pitch. (b) SEM close-up of a single tip. (c) Schematic of a single 800 nm pulse interacting with a single silicon tip. λ is the laser wavelength, T is the pulse duration, and E is laser energy.

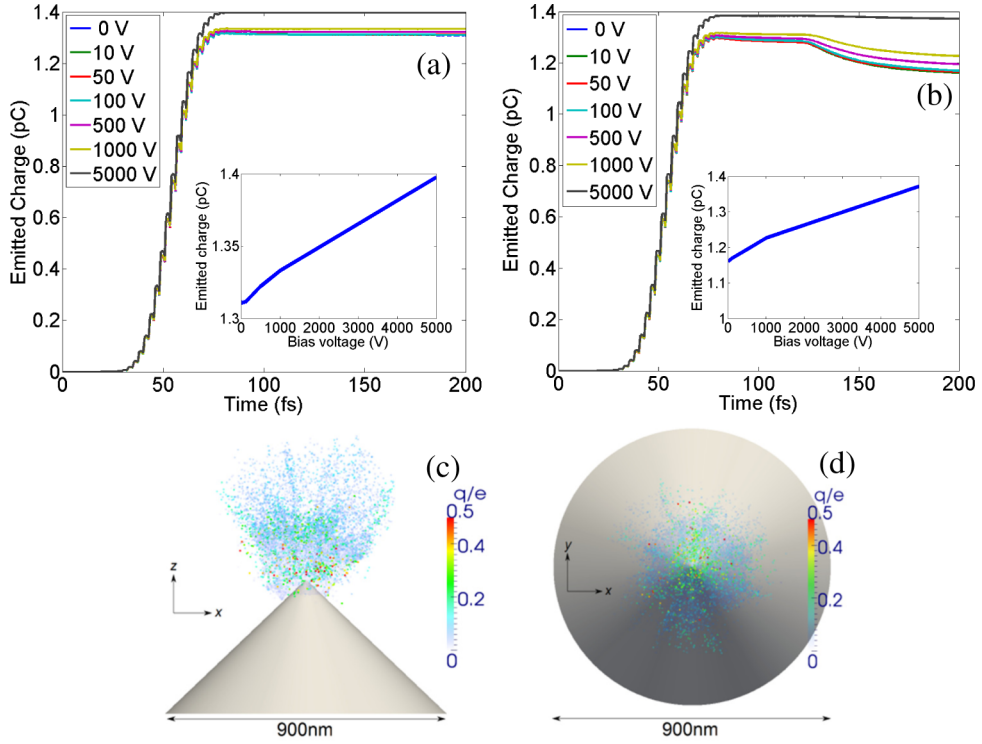

Figure 2. Emitted current from a single tip multiplied by 2200 versus time for different anode voltages: (a) without and (b) with considering space-charge and image charge effects. If the electron returns to the surface, it is assumed to have a recombination rate of 0.7.[9] The applied DC field reduces the collision rate of the emitted electrons to the surface, thereby increasing the total amount of emitted charge. This is more prevalent when image charge effects are considered. (c, d) Emitted charge profile due to field emission at the tip with 70 V anode bias at t = 120 fs: (c) side-view and (d) top-view of the charge profile including space-charge and image charge effects. The density of points and the color code represent the charge density. Each point represents a charge emitted at a specific time step due to the existing local electric field. Roughly 1000 electrons are emitted from each tip with uncertainties in the exact emission position and time. Hence, there exists a charge distribution around the tip which is modeled and visualized by more than 50 000 particles with charges equal to fractions of an electron charge. The red dots represent regions with highest charge density.

excitation parameter range where strong-field emission occurs and charge effects are negligible.

Beyond increasing the spectral efficiency of a planar silicon cathode, the multiphoton process of emission and ultimately strong-field emission using near-IR pulses leads to a natural localization of electron emission. For instance, assuming a three-photon absorption process is necessary to liberate an electron, with a factor of 10 field enhancement occurring only near the end of the tip, electron emission there increases by a factor of 1 million with respect to regions with no enhancement. This leads directly to a nanoscale confinement of electron emission,[16] circumventing the need of extra complications in fabrication, such as the use of a mask layer to create structured electron beams. Furthermore, by pushing the local electric field intensities at the tip surface high enough using near-IR pulses, the tunneling, or strong-field regime of emission is achieved (Figure 1). This opens up applications to attosecond science, as the physics describing this emission implies that the electrons are being emitted over a narrow subcycle region of the driving pulse's electric field. The tips

dx.doi.org/10.1021/nl501589j | Nano Lett. 2014, 14, 5035−5043

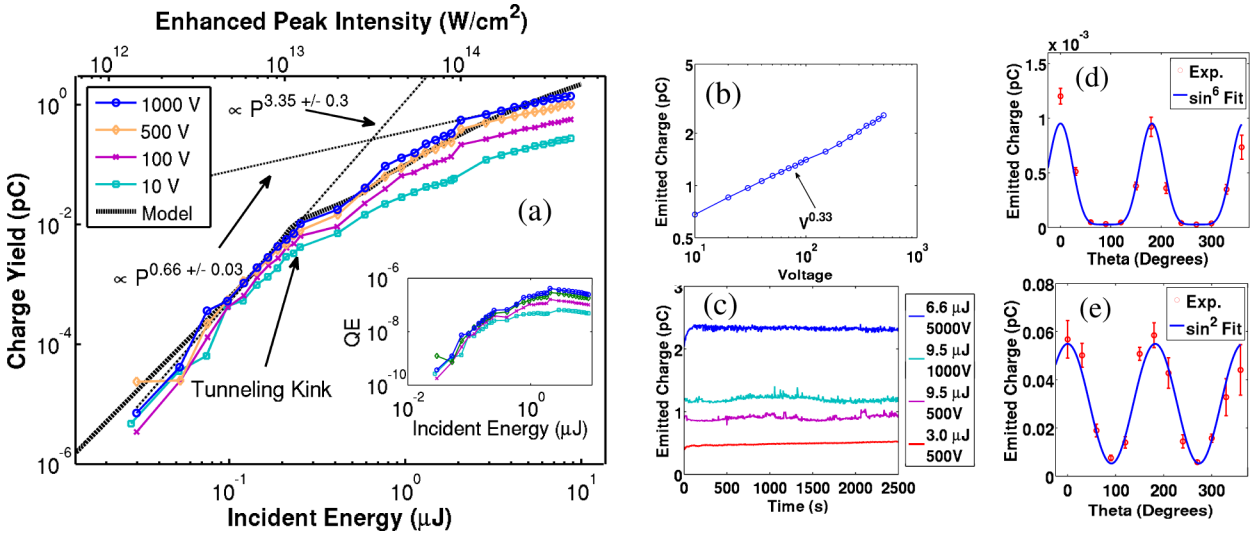

Figure 3. Experimental results: (a) Emitted charge and overall quantum efficiency (QE) as a function of laser pulse energy for various anode bias voltages. A 3-photon emission growth is shown in current at low intensities, followed by a tunneling kink at an enhanced peak intensity near 1×10^{13} W/cm^2. (b) Log–log plot of emitted charge versus bias-voltage at fixed incident pulse energy of 10.8 μJ. The <1 voltage dependence slope indicates that the emission is not fully space-charge limited. (c) Stability of emitted current from the photocathode over time showing stable output. In (d) and (e) the polarization was changed continuously from 0° (along the tip) to 360° to show the effect of polarization on charge yield. The bias voltage was maintained at 10 V for these measurements. (d) At an enhanced peak intensity of 5.7×10^{12} W/cm^2, the current increases with the third power of pulse energy. (e) At an enhanced peak intensity of 27.5×10^{12} W/cm^2, γ is less than 2 and the emission increase linearly with intensity.

could thus be used as a near-field (i.e., near the tip) attosecond probe with increased signal yield due to multiplexing.[1,17]

Expanding on the experimental results of single tip emission,[5,7,8,11,12] we begin by modeling the emission from a single tip in the time domain using 35 fs 800 nm pulses at 6° grazing incidence (Figures 1c and 2). The model computes the field enhancement of the laser and static anode bias voltage, while also performing particle tracing. The simulations are based on the Fowler–Nordheim (FN)[18] model of electron emission, applicable in the tunneling regime,[19] accounting for space-charge and Coulomb-blockade effects by adding the fields of a moving charge to the time domain Maxwell solver.[20,21] The simulation challenges are the range of length and time scales involved, the electron dynamics in the presence of static as well as ultrahigh frequency fields, the electron–electron interaction (i.e., space-charge effects), and the Coulomb blockade of the electron bunch induced on the surface (for details on the simulation method, refer to the Methods section). Figure 2a and b shows the modeled current from a single tip (multiplied by 2200 to match the number of tips illuminated in the experiment) without and with space charge, respectively. The effect of space charge is small, reducing the total emitted electrons by 14% for a 10 V bias compared to a bias of 5 kV across a 3 mm anode to cathode gap (Figure 2a–b). Particle tracing shows that this is due to a rapid spread of electrons leaving the tip, thus reducing space-charge effects that would otherwise drive the electrons back to the cathode. As seen from the obtained emitted charge simulations, the space-charge consideration leads to a small recombination rate for the electrons (i.e., electrons reabsorbed by the cathode), which vanishes with an increase in anode voltage. This confirms the intuition used by Bormann et al.[5] to describe the high current yields observed from a single Au tip and is within the range of fields experimentally tested, far below the damage threshold (Figure S1).

Our experimental results indicate that the high electric field of the ultrashort laser pulses combined with the field enhancement of the nanosharp high-aspect-ratio silicon tip array resulted in large current emission at small laser energies, pC emitted charge at μJ incident energy (Figure 3a). While the overall quantum efficiency (QE, inset Figure 3a), calculated simply as the number of electrons emitted per incident photon, does not exceed 10^{-6}, this is high considering that only a very small fraction of the emitter surface is utilized, as the tip diameter is sub-10 nm and the tip spacing is 5 μm (i.e., about one 3 millionth of the total array area emits electrons). The emission is also greatly enhanced as compared to our measurements on planar Si, yielding just 1 fC of charge for 5 μJ incident energy corresponding to a QE of 10^{-10}. Assuming the same field enhancement at the tip, it is estimated that the overall QE could be further increased by more than 1 order of magnitude by reducing the tip spacing. At low energy (<0.2 μJ), the charge yield has a slope of ~3.4 ± 0.3 on a log–log scale (i.e., $\propto P^{3.4}$ pC/μJ$^{3.4}$ as shown in Figure 3a, where P is the pulse energy). This matches closely to the expected slope of 3 for a three-photon absorption process, given that the electron affinity of Si is 4.05 eV, and the photon energy at 800 nm is 1.55 eV. (The convention for slope meaning a power law dependence will be used throughout the remainder of the paper). Around 0.2 μJ, there is a kink in the log–log plot that is observed at all bias levels. For the case of single tips, it has been observed that such a bendover in current yield occurs near a Keldysh parameter of $\gamma = (\phi/2U_p)^{1/2} \approx 2$,[5,7,19] where ϕ is the material work function, and U_p is the ponderomotive potential of the local laser field:

$$U_p = \frac{q^2 F_0^2}{4m\omega^2} \quad (1)$$

In eq 1, q is the electron charge, F_0 the peak electric field strength, m the electron mass, and ω the angular frequency of the laser.

To simulate total electron yield as a function of incident intensity, a model based on strong-field perturbation theory[19,22]

dx.doi.org/10.1021/nl501589j | Nano Lett. 2014, 14, 5035–5043

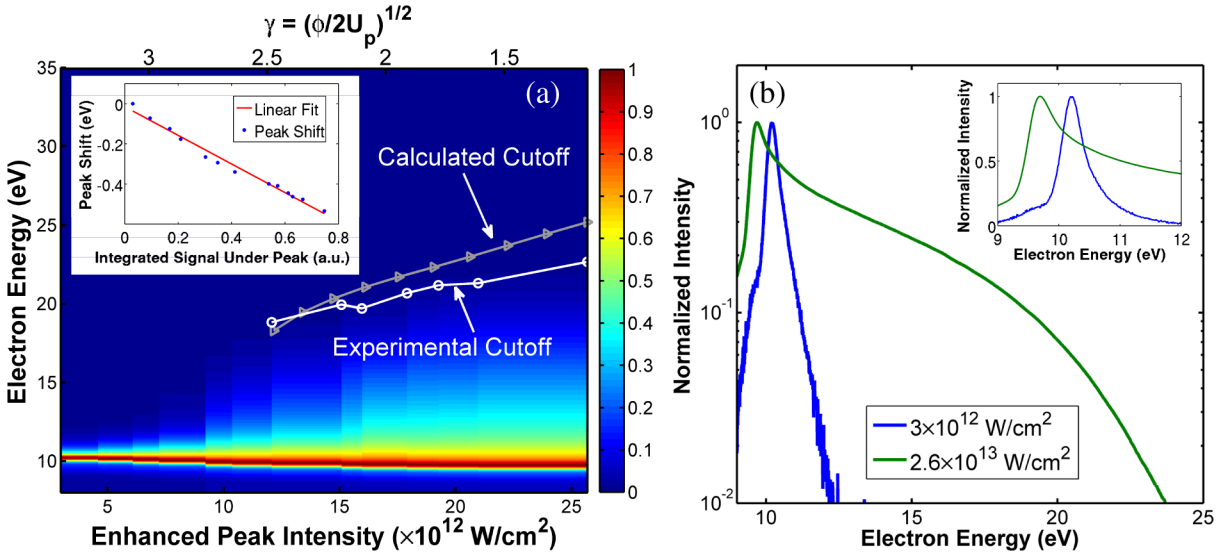

Figure 4. Electron energy spectra. In (a) normalized spectra are plotted as a function of increasing pulse energy to show the extension of the high-energy plateau as laser energy is increased. The 10 eV offset in the spectra is due to the applied bias between the sample and entrance aperture of the spectrometer. For intensities beyond the observed current kink, the experimental and calculated cutoffs are plotted. The calculated cutoff uses a Simpleman model incorporating the simulated electric field profile along the axis of the tip. The inset shows the energy shift of the peak near 10 eV as a function of current underneath the peak region of the spectra. In (b) spectra are selected from the lowest and highest pulse energy points tested. The inset contains a zoom on the low-energy peak of the spectra on a linear scale.

was implemented (described further in the text). Averaging effects due to both pulse duration and beam shape on the emitter surface were accounted for. This result is compared to the experimental data in Figure 3a. A good fit is obtained across all incident laser pulse energies for the highest bias voltages, where a deviation is only observed at the highest incident pulse energies. An electric field enhancement factor of ∼10.5 was used to account for an enhanced peak intensity at the tip relative to the incident peak intensity of the pulse, which is in good agreement with the 9.4 enhancement factor found with the electromagnetic model (Figure S2). For peak intensities beyond the kink (i.e., $\gamma < 2$), the electrons begin to tunnel into vacuum faster than they can oscillate back into the tips,[5,10] and the emission follows a time-averaged Fowler−Nordheim model.[19] This regime is commonly referred to as the strong-field or tunnelling regime of electron emission. As shown later in the text, while the initial slope change is due to the transition to the tunneling emission regime, the final charge yield at the highest incident energies is reduced from the expected value by as much as 80% for a bias of 10 V due to the onset of a space-charge induced virtual cathode (Figure 3a).

To ensure the emission is due to electric field enhancement at the tip and not just an increase in surface area (i.e., extra emission along the shank of the tips), the charge yield is measured while rotating the polarization angle (θ) at a fixed bias of 10 V (Figure 3d−e). For both low and high pulse energies, peak emission occurs when the polarization is parallel to the axis of the tip, and minimum emission for the orthogonal polarization. For the case of high pulse energies, the polarization followed a $\sin^2(\theta)$ dependence, while for low energies that of a $\sin^6(\theta)$ dependence, corresponding to the tunneling and multiphoton emission regions, respectively.

Figure 3c shows four different cathode currents on four different sample locations with the beam being unblocked at time 0 s at an unexposed area. All four curves show stable current emission after 8 million pulses, which is important for electron source applications where surviving millions of cycles at high charge output is required. The lowest curve in Figure 3c has lower noise than the others and is slightly rising. This is because field emission current is highly nonlinear with respect to the photon energy, and the activation of the cathode takes longer at lower fields.[3] The highest curve in Figure 3c shows an average 2.3 pC electron emission per pulse. SEM images taken after exposing the tips to 8 million pulses showed no measurable difference between the nonexposed tips and the exposed tips for laser energy pulses below 10 μJ. For laser pulses with 10.8 μJ energy, some dulling of the tips is observed, and the tip radii spread is also increased (Figure S3). When the energy of the laser pulses is over 20 μJ, the tips are ablated, leaving a ∼85 μm by 1800 μm mark in the samples that matches the laser spot size (Figure S1).

A second hallmark of strong-field, or tunneling, emission is found in the measured electron energy spectra, shown as a function of increasing laser intensity in Figure 4. Due to a narrow emission window near the peak of the electric field and subsequent acceleration and rescattering with the tip, the electron spectrum develops an asymmetric structure having a sharp, low-energy direct electron peak followed by a broad plateau extending out to high energies.[7,8,11,12] Classically speaking, an electron born within a laser field alone can at most be accelerated to an energy of $2U_p$. However, with the inclusion of a rescattering boundary, the plateau cutoff energy can exceed $10U_p$.[23,24]

An electron time-of-flight (TOF) spectrometer was used to study the electron energy spectra as a function of incident drive intensity at 800 nm (see Methods). The results of this scan show a sharp (<1.5 eV fwhm peak width) low-energy peak with a high-energy plateau extending to around 12 eV beyond the low-energy peak at the highest pulse energy tested. To ensure the high-energy plateau is indeed due to laser acceleration after emission, space-charge broadening must be ruled out. The single-tip modeling results described previously (Figure 2) show that pulse spreading indeed occurs with the inclusion of space-charge; however the high-energy plateau was still

dx.doi.org/10.1021/nl501589j | Nano Lett. 2014, 14, 5035−5043

dominated by laser accelerated electrons for charge yields exceeding 1 pC, while the yield in the spectral measurements shown in Figure 4 did not exceed 50 fC. While this rules out such effects in the single-tip limit, the substrate and neighboring charges may also influence the spectra. Femtosecond electron pulse spreading from a planar cathode due to electron−electron interactions has been shown both theoretically and experimentally to scale as the square root of the number of particles in the electron bunch and be inversely proportional to the electron bunch radius.[25,26] Passlack et al.[25] experimentally demonstrated that for an electron pulse with a group velocity corresponding to 0.18 eV, the pulse broadening did not exceed 300 meV for more than 75 000 electrons per pulse and an initial bunch radius of 350 μm. Accounting for the differences in initial bunch radius based on the beam profile used, even a conservative estimate does not indicate broadening the electron pulse by more than 2 eV at the highest yield measured.

To determine the plateau cutoff extension described by laser acceleration, a semiclassical model to analyze the cutoff scaling as a function of laser intensity was used. The enhanced peak intensity was calibrated by matching the current scaling measured at the spectrometer (see Methods) to the measurements in Figure 3a. Using this calibrated peak intensity, a cutoff scaling analysis was then performed by using the well-established Simpleman model[6,7,12] for enhanced peak laser intensities at and exceeding the observed kink in current yield (i.e., the tunneling regime). The details of the calculation are outlined in ref 9, where we have replaced the dipolar decay function describing the electric field profile with the simulated profile from the electromagnetic simulations described earlier. Also, the oxide layer is assumed to be negligible (see Methods). To account for the DC bias in the simulation, the solution is shifted by 10 eV. Space charge is neglected in this calculation, following the previous discussion. The cutoff value was defined as being the energy where the condition $I(E) = 0.1I(E/2)$ is satisfied, where I is the spectrum intensity and E the electron energy. The results are overlaid with the energy spectra in Figure 4a and compared to the measured cutoff values using the same condition. The calculated cutoff values are offset to slightly higher energies, with a slightly increased slope relative to the measured values. Overall, the agreement between the measured and the predicted cutoff values is reassuring given that the peak intensity was calibrated using the kink in current yield, an entirely separate measurement, rather than as a free parameter to achieve the best fit.

The absolute value of the cutoff using this method is sensitive to the exact spectral shape. Since the semiclassical model results in spectra having much steeper cutoff than those observed experimentally, it is difficult to find and absolute match between calculated and measured values. However, the difference in slope is more interesting as this points to a deviation between the modeled and actual field decay away from the tip apex. The calculations here already show a reduced slope for the modeled field decay as compared to the case of a homogeneous electric field due to the fact that the electron excursion starts to be on the order of the field decay length, resulting in a minimum adiabaticity parameter[12] $\delta \approx 15$. While not deep into the subcycle regime where the adiabaticity parameter is much less than 1 and the cutoff scales linearly with the field,[12] the overall reduction in cutoff energy can be quite severe much before this regime is reached (Figure S4).

Laser-induced cutoff scaling also indicates that the emission process is prompt with respect to the driving electric field, as the laser can only accelerate electrons that are present within the duration of the laser pulse itself. Preliminary cross correlation electron emission measurements using two-color pulses further demonstrate the prompt nature of the electron emission and laser-induced spectral shaping (Figure S5). Measuring electron emission as a function of delay between a 1 μm pulse and 2 μm pulse incident on the tips resulted in a sharp current spike tens of femtoseconds in duration that shows no evidence of a long-lifetime pedestal on either side. Furthermore, when the pulses were overlapped, the cutoff was extended by around 7 eV (Figure S5b), while the bandwidth of the low energy spectral peak was effectively unchanged (Figure S5a). This is shown to be due to an increase in ponderomotive acceleration in the presence of a two-color field.[24] Such results indicate the possibility of tailoring laser waveforms to engineer emitted electron spectra. The reader is directed to the Supporting Information for a more detailed discussion of these results.

Another feature that stands out from the electron spectra is the slight loss in energy of the main spectral peak as the intensity is increased. If the effect is solely due to changing ponderomotive potential, then the shift should vary linearly with peak intensity, which was not found to be the case. The single tip model at the beginning of the paper indicates that image charge effects from the tip alone can contribute significantly to electron deceleration and recombination with the tip surface at pC level yields across the entire array. In recent years, observations of peak shifts in photoemission due to image-charge effects have been studied in detail across a variety of emission levels.[27,28] Zhou et al.[28] show experimentally and theoretically that the image charge-related shift from a planar conductive sample is due mostly to the amount of charge in the bunch, and shifts the mean energy linearly with respect to the total number of electrons in the bunch. A simple analysis shows that the main spectral peak indeed shifts linearly to lower energies with respect to the number of charges in the peak, but not the total charge (Figure 4a inset). This interpretation is also consistent with the idea that the fast moving electrons quickly escape the low-energy bunch after laser acceleration, and contribute minimally to the peak shift.

At higher incident energies, the anode bias voltage had a significant effect on the emitted charge (Figure 3a). At 9.3 μJ incident energy, the emitted charge is 0.27 pC with 10 V anode bias and 1.4 pC with a 1000 V anode bias. From finite element modeling, the local electric field from the anode bias (~3 MV/m at 500 V anode bias) is 3−4 orders of magnitude lower than the peak field from the incident laser (~6 GV/m before enhancement at ~11 μJ pulse), meaning there should be no noticeable increase in electric field and emitted current due to the increase in anode bias. Also, the slight reduction in emission due to space-charge effects around a single emitter, as outlined in Figure 2, does not account for the extent of anode bias dependence observed experimentally. With this in mind, it is necessary to turn to a macroscopic space-charge model that accounts for the charge from neighboring emitters.

To model the emission across the entire pulse energy range tested, a method employing strong-field perturbation theory was used, which has been successful in modeling such emission from atomic systems[22,23] and more recently nanotips.[5,19] The equation describing the ionization process is given, to first order, as

dx.doi.org/10.1021/nl501589j | Nano Lett. 2014, 14, 5035−5043

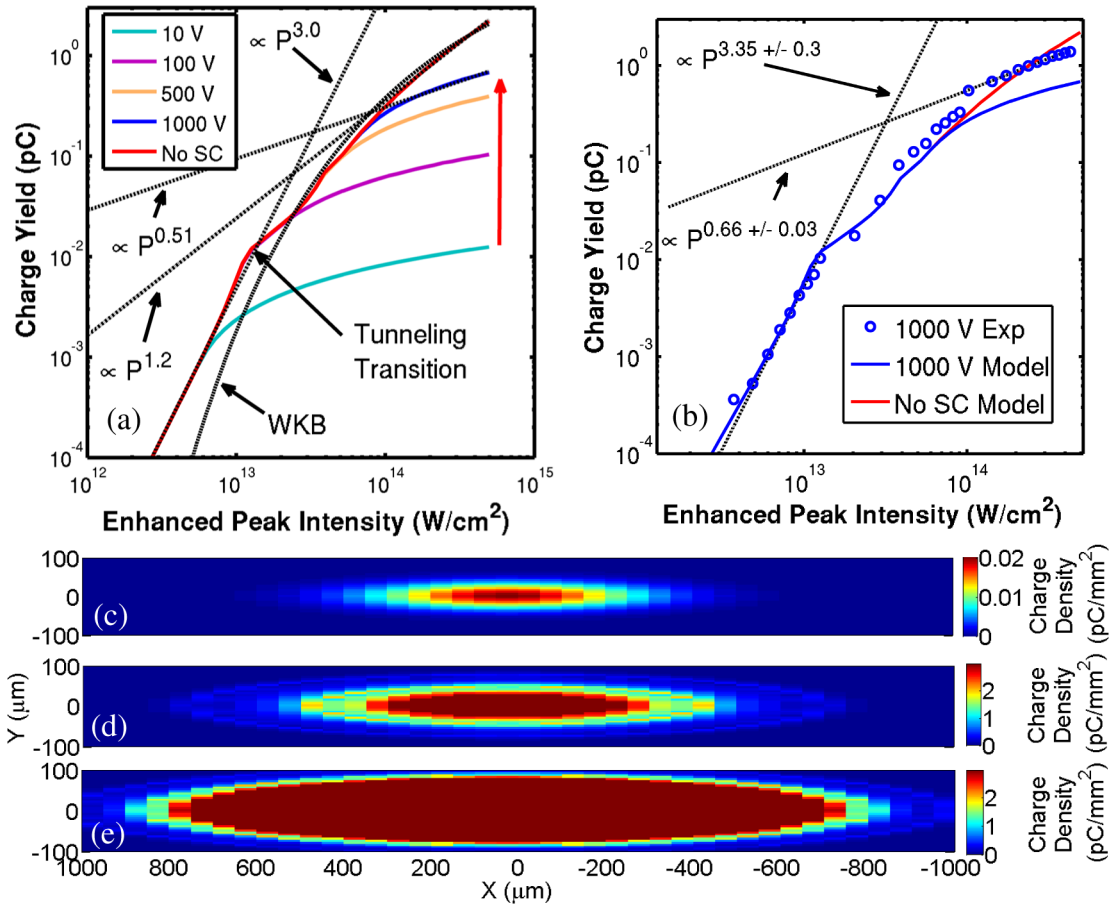

Figure 5. Modeled and calculated results. (a) Model results of the emitted current as a function of laser pulse energy and bias voltage. No SC refers to the case where no space-charge effects were considered ($Q_{crit} \rightarrow \infty$). The red arrow indicates increasing Q_{crit}, i.e. increasing virtual cathode limit, as a function of bias. As expected, the data fits well to a spatially and temporally averaged WKB model after the tunneling kink. (b) The experimental data at 1 kV is compared to the model with and without consideration of the virtual cathode limit. At 1000 V, the ultimate power dependence slope is 0.51, compared to 0.66 in the experiment and 1.2 when neglecting space-charge. (c, d, e) Calculated electron beam profiles at the anode plate for 0.1, 1.6, and 10 μJ pulse energies with a bias voltage of 1000 V. Due to saturation at Q_{crit}, the model shows that the effective emitter area grows, and the electron bunch develops a top-hat shape.

$$I \propto \frac{1}{\hbar}\int_0^\infty |M_p^{(1)}|^2 dp \tag{2}$$

where

$$M_p^{(1)} = \frac{-i}{\hbar}\int_{-\infty}^{\infty} dt\, \exp\{iS_p(t)/\hbar\}\langle p + qA(t)|qzF(t)|\Psi_0\rangle \tag{3}$$

Here, S_p is the action due to the laser field and is given by

$$S_p(t) = \frac{1}{2m}\int^t dt\{p + qA(t)\}^2 \tag{4}$$

In eqs 3–4, $A(t)$ is the magnetic vector potential, Ψ_0 the ground state before excitation, p the final momentum, $F(t)$ the electric field of the laser pulse, $M_p^{(1)}$ the transition amplitude of the electron to final momentum p, and m the electron mass. In eq 3, $F(t)$ is taken to be a Gaussian pulse having a 35 fs full width at half-maximum (fwhm) in intensity. There are a few assumptions in this expression. First, supply is not accounted for, which means that the expression is only accurate when the electron emission is not limited by the electron supply from the conductor. Second, the emission is assumed to be dominated by electrons located just above the conduction band of Si, having and electron affinity of 4.05 eV. Lastly, the electric field inside of the conductor is neglected, meaning the spatial part of the matrix element is only calculated over the vacuum half-space.

A key feature of this emission model is accounting for the possibility of multiphoton emission as a function of laser energy at low intensities, unlike a pure FN model that underestimates electron emission in this region by several orders of magnitude. Furthermore, the model includes a description of how the emission transitions from multiphoton absorption to quasi-static tunneling. As a consequence of the electron being emitted into a strong laser field, the ponderomotive potential, U_p, adds to the effective work function of the boundary.[29] This means that as the laser strength increases, higher order photon absorption becomes necessary in order to liberate an electron. When this happens, the slope of the yield bends over, matching more closely to a time-averaged Wentzel–Kramers–Brillouin (WKB) tunneling emission rate (Figure 5), justifying the use of the FN model at high intensities.

To model the charge density across the surface of the cathode, a Gaussian driver beam of 90 μm fwhm was projected across the emitter surface at an angle of 84° matching the experimental beam size and angle. The beam spot was then divided into grids having a constant intensity, and the strong field emission model described earlier was used to determine

dx.doi.org/10.1021/nl501589j | Nano Lett. 2014, 14, 5035–5043

the differential current from each grid point. For the case of a 1 kV bias, aside from the very highest intensities, the model describes the total current yield profile with surprising accuracy (Figure 5b) as only the field enhancement and constant prefactor were used for fitting.

From the single tip model, we find that at high laser fields the transverse size of the charge cloud rapidly diverges after the total charge emission (Figure S6). The results show that less than 1 ps after the charge emission (compared to ∼1 ns of flight time to reach the anode at a 3 mm spacing), the cloud transverse size is as large as the lattice constant, i.e., 5 μm. This could easily lead to a global space-charge effect where the extraction bias is screened by the emitted current bunch. The simplest approach to account for global space-charge is to assume that the charge from each emitter converges into a sheet of charge just above the cathode surface after emission (Figure S6). To account for space charge, the differential charge from each spatial grid point was not allowed to exceed the critical charge, given by

$$Q_{\mathrm{crit}} = \frac{VA_{\mathrm{g}}\epsilon_0}{d} \tag{5}$$

where V is the bias voltage, A_{g} the grid area, ϵ_0 the permittivity of free space, and d the anode-to-cathode spacing. The space-charge limit provided in eq 5 is more applicable than the Child−Langmuir current limit for ultrafast cathodes, where the current is bunched into a thin sheet rather than spread across the entire anode−cathode gap.[30] While this analysis ignores the near-field tip enhancement, this should decay back to the solution for a planar sheet of charge within hundreds of nanometers of the tip surface (Figure S7c), making expression in eq 5 relevant for electron transport in the vacuum. The induced virtual cathode voltage used to determine Q_{crit} also naturally accounts for an induced image charge potential (assuming a planar image charge surface). The results of this model effectively describe an electron pulse that first saturates in the center, while the wings continue to increase, thus leading to a larger effective spot size and a top hat profile. Model results for no space-charge limit (i.e., $Q_{\mathrm{crit}} \rightarrow \infty$), 10 V, 100 V, 500 and 1000 V DC bias are given in Figure 5.

The model results match many of the features observed in the experimental data. At low intensities, the emission follows a 3-photon absorption process, where there is no dependence on bias voltage. At higher intensities, when the current yield goes beyond the space-charge limit in the center of the laser spot, the current begins to saturate depending on the bias voltage applied (Figure 5c−e). Beyond a 500 V bias voltage, the bend over due to a transition to the tunneling regime is prevalent, followed by a very gradual transition to space-charge saturation at a higher current yield.

However, overall the model seems to underestimate the current limit for each voltage. For example, without the space-charge limit, the ultimate slope at the highest current yield is ∼1.2 vs ∼0.51 for a 1 kV bias in the model as compared to ∼0.66 for the experimental data. Also, in the experimental results, the tunneling kink was clearly observed for every bias level. As noted in Valfells et al.,[30] the major limitation of this calculation is that it does not account for the initial velocity of the charge leaving the cathode. This leads to an underestimation of the total current limit as the initial energy of the electrons lead to larger beam radii and the requirement for higher potentials to prevent their escape. From the electron spectroscopy results (Figure 4a−b), a large spread in longitudinal energy was observed, and the single tip particle tracing indicates significant transverse momentum, both of which explain charge yields exceeding the limit imposed by eq 5.

The results show an ultrashort electron pulse emission from large structured field emission cathodes including micro and macroscopic effects, enabling many new avenues for physics and engineering. We also clearly demonstrate the transition from the multiphoton to the strong-field tunneling regime across a massive array of tips, while accounting for space-charge effects. Modeling of the current yield at high field strengths demonstrated rapidly diverging electron trajectories coming from a highly localized volume near the tip apex, with little space-charge reduction of current yield. However, as the electrons form a current sheet above the emitter, extraction was found to be limited by the formation of a virtual cathode. Such space-charge limitations can be easily mitigated when used in a RF photoinjector due to the high RF extraction field. The cathodes are also fabricated in standard CMOS processes and are stored in air at standard conditions before testing at high vacuum (10^{-8} Torr), which is a major advantage over reactive low work function cathodes that are fabricated and stored in ultrahigh vacuum conditions. Tip arrays are highly uniform, standard deviation of less than 1 nm tip radius of curvature, from die to die on a wafer but also from wafer to wafer; emitter multiplexing has major advantages over reactive low work function cathodes or cathodes made of just a single tip because of the confined structured electron beam that the emitter arrays produce.

Methods. For the simulation of optical field propagation, an in-house time-domain Maxwell solver based on the Discontinuous Galerkin Time Domain (DGTD) method is developed. The software is written in C++ and is efficiently parallelized using the Message Passing Interface (MPI) library. The geometry of the field emitter is drawn and discretized using the Gmsh (geuz.org/gmsh/) software and the DUNE library (www.dune-project.org) is utilized for the mesh and grid management. The whole geometry shown in Figure S2 contains 157 093 tetrahedral elements. The n-doped silicon, 10^{15} cm^{-3}, emitter is modeled using the Drude model. By utilizing the same libraries, we also developed a parallel Poisson solver for calculating the DC field distribution around the field based on the FEM. The DC simulation geometry is discretized to 800 000 elements, and the field profile shown in Figure S7 is obtained. In the DC simulation, n-doped silicon is considered as a perfect conductor. We superpose the two fields on the surface of the emitter to calculate the emitted charge using the FN model. This leads to the charge distribution shown in Figure 2c−d. In order to capture the space-charge and Coulomb-blockade effects in the simulation, the field of the emitted particles are divided into radiated field and static (Coulomb) field. The radiated field is added to the propagating fields of the DGTD method and propagated with time in the region around the tip. For considering the Coulomb repulsion effect on the particle motion as well as the field emission current, point-to-point implementation is utilized. A crude usage of point-to-point formulation leads to large computation costs. However, due to the strong decay of these fields with distance, considering the fields of the particles in the close proximity of the observation point suffices. For the charges residing close to the surface, a modified Coulomb field considering the image charge effect is used.

dx.doi.org/10.1021/nl501589j | Nano Lett. 2014, 14, 5035−5043

Finally, the electrons are accelerated in the spatial field calculated from the superposition of optical, DC, and space-charge fields. For this purpose, the equation of motion is integrated over time using a fourth order Runge−Kutta method.

To characterize the electron energy spectrum, a time-of-flight (TOF) energy spectrometer having a field-free drift length of ∼35 cm with μ-metal shielding was used. At the end of the drift tube, the electrons are detected by a microchannel plate (MCP) detector followed by a collector anode. Given the drift length and rise time of the MCP/collector, the energy resolution of the spectrometer is ∼107 meV at a central energy of 10 eV. The samples were mounted in front of the entrance aperture of the detector at a grazing incidence angle of 6°, and a bias voltage of 10 V was applied to the substrate in order to sweep the low-energy electrons from the surface (Figure 4). The cathode was excited with 35 fs, 800 nm laser pulses at 3 kHz repetition rate from a regeneratively amplified titanium sapphire oscillator seed. The laser pulses hit the samples at an 84° grazing incidence, creating a 765 μm by 80 μm ellipse that bathes ∼2220 tips.

When taking electron spectra, a transimpedance amplifier (Femto DDPCA-300) was connected between the sample and ground to simultaneously measure the total current yield of the sample. This provided an absolute measurement of current not dependent on spectrometer efficiency. To avoid saturation effects on the MCP in the TOF spectrometer, only total charge yields up to ∼50 fC were tested. A zero-order half-wave plate was used to perform the polarization measurements.

The cathodes are fabricated from an n-Si (∼5 Ω-cm) 150 mm diameter wafer. An array of concentric silicon nitride (250 nm) and silicon dioxide (500 nm) thin films are patterned with projection lithography and dry etched. The pillars are formed by deep reactive-ion etching, and thermal oxidation thins the pillars while also forming the nanosharp tip by a stress limited process. The oxide and nitride are removed by wet chemical release and then dipped in 2% hydrofluoric acid immediately before being placed in the vacuum (10^{-8} Torr) testing chamber, leaving over half a million highly uniform 5 μm hexagonally packed arrays of single-crystal silicon pillars about 38 μm tall and 900 nm wide, each topped by an ultrasharp tip (Figure 1a). The tip radii spread across the array was estimated by conducting metrology on high-resolution FE-SEMs (Figure 1b) from 30 tips selected at random with an average radius of curvature of 4.4 nm with a standard deviation of 0.6 nm (Figure S3a), in contrast with the wide tip radii distribution commonly associated with nanosharp silicon tip arrays.[31] After prolonged exposure to 10.8 μJ laser pulses and 500 V anode bias; we found an average radius of 7.8 nm and a standard deviation of 1.2 nm, number of samples, n = 29 (Figure S3b). The blunter tips with wider size spread are a result of the very high peak fields and currents interacting with the tips. However, the performance of the arrays had no noticeable degradation at 10.8 μJ, and at energies under 10 μJ, there was no visible damage.

The cathode chip was connected to ground through a picoammeter, Keithley 6485, while the anode, i.e., a 0.25-in. diameter plate placed 3 mm above the sample, was biased at 10−1000 V using a source-measuring unit (SMU) Keithley 237 (Figure S8). For anode biases >1000 V, a Keithley 248, was used. The signal collected via LabView is DC current through the cathode and anode resulting in average current measurements over a series of electron pulses with 3 kHz repetition rate. The current is then converted to emitted charge per pulse by dividing the average current value by the repetition rate of the laser.

■ ASSOCIATED CONTENT

Ⓢ Supporting Information

Tip damage results, further discussion of electromagnetic simulations, cutoff scaling simulation results, two-color measurement results, tip radii distribution measurements, and simulated electron position and momentum distributions. This material is available free of charge via the Internet at http://pubs.acs.org.

■ AUTHOR INFORMATION

Corresponding Author

*Tel. +1-617-2530730; e-mail: Velasquez@alum.mit.edu.

Author Contributions

M.E.S. and P.D.K. contributed equally on this work. F.X.K. and L.F.V.-G. helped design the experiment. A.F. did the finite element analysis modeling. M.E.S. helped design the experiment, fabricated the devices, and split experimental testing and writing the manuscript with P.D.K. P.D.K. helped design the experiment and split experimental testing and writing the manuscript with M.E.S. P.D.K., P.R.K., G.L., and J.M. designed and implemented the two-color experiments. All authors edited the manuscript.

Notes

The authors declare no competing financial interest.

■ ACKNOWLEDGMENTS

The device fabrication was done in the Microsystems Technology Laboratories, MIT. We would like the thank W. Graves, E. Nanni, and R. Hobbs from MIT for the helpful discussions. This work was funded by the Defense Advanced Research Projects Agency/Microsystem Technology Office (DARPA/MTO) under contract N66001-11-1-4192 (program manager D. Palmer). Any opinions, findings, and conclusions or recommendations expressed in this publication are those of the authors and do not necessarily reflect the views of the US Government and therefore, no official endorsement of the US Government should be inferred.

■ REFERENCES

(1) Baum, P.; Zewail, A. H. *Proc. Natl. Acad. Sci. U.S.A.* **2007**, *104*, 18409−18414.
(2) Graves, W. S.; Kärtner, F. X.; Moncton, D. E.; Piot, P. *Phys. Rev. Lett.* **2012**, *108*, 263904.
(3) Guo, Q.; Takahashi, K.; Saito, K.; Akiyama, H.; Tanaka, T.; Nishio, M. *Appl. Phys. Lett.* **2013**, *102*, 092107−092107-4.
(4) Hommelhoff, P.; Sortais, Y.; Aghajani-Talesh, A.; Kasevich, M. A. *Phys. Rev. Lett.* **2006**, *96*, 077401.
(5) Bormann, R.; Gulde, M.; Weismann, A.; Yalunin, S. V.; Ropers, C. *Phys. Rev. Lett.* **2010**, *105*, 147601.
(6) Dombi, P.; Hörl, A.; Rácz, P.; Márton, I.; Trügler, A.; Krenn, J. R.; Hohenester, U. *Nano Lett.* **2013**, *13*, 674−678.
(7) Piglosiewicz, B.; Schmidt, S.; Park, D. J.; Vogelsang, J.; Groß, P.; Manzoni, C.; Farinello, P.; Cerullo, G.; Lienau, C. *Nat. Photonics* **2014**, *8*, 37−42.
(8) Yanagisawa, H.; Hengsberger, M.; Leuenberger, D.; Klöckner, M.; Hafner, C.; Greber, T.; Osterwalder, J. *Phys. Rev. Lett.* **2011**, *107*, 087601.
(9) Keathley, P. D.; Sell, A.; Putnam, W. P.; Guerrera, S.; Velásquez-García, L. F.; Kärtner, F. X. *Ann. Phys.* **2013**, *525*, 144−150.
(10) Keldysh, L. V. *Sov. Phys. JETP* **1965**, *20*, 1307−1314.

(11) Krüger, M.; Schenk, M.; Hommelhoff, P. *Nature* **2011**, *475*, 78−81.
(12) Herink, G.; Solli, D. R.; Gulde, M.; Ropers, C. *Nature* **2012**, *483*, 190−193.
(13) Wong, L. J.; Fallahi, A.; Kärtner, F. X. *Opt. Express* **2013**, *21*, 9792−9806.
(14) Huang, S.-W.; Cirmi, G.; Moses, J.; Hong, K.-H.; Bhardwaj, S.; Birge, J. R.; Chen, L.-J.; Li, E.; Eggleton, B. J.; Cerullo, G.; Kärtner, F. X. *Nat. Photonics* **2011**, *5*, 475−479.
(15) Smorenburg, P. W.; Op't Root, W. P. E. M.; Luiten, O. J. *Phys. Rev. B* **2008**, *78*, 115415.
(16) Ropers, C.; Solli, D. R.; Schulz, C. P.; Lienau, C.; Elsaesser, T. *Phys. Rev. Lett.* **2007**, *98*, 043907.
(17) Barwick, B.; Flannigan, D. J.; Zewail, A. H. *Nature* **2009**, *462*, 902−906.
(18) Fowler, R. H.; Nordheim, L. *Proc. R. Soc. London, Ser. A* **1928**, *119*, 173−181.
(19) Yalunin, S. V.; Gulde, M.; Ropers, C. *Phys. Rev. B* **2011**, *84*, 195426.
(20) Paarmann, A.; Gulde, M.; Müller, M.; Schäfer, S.; Schweda, S.; Maiti, M.; Xu, C.; Hohage, T.; Schenk, F.; Ropers, C.; Ernstorfer, R. *J. Appl. Phys.* **2012**, *112*, 113109.
(21) Hoffrogge, J.; Stein, J. P.; Krüger, M.; Förster, M.; Hammer, J.; Ehberger, D.; Baum, P.; Hommelhoff, P. *J. Appl. Phys.* **2014**, *115*, 094506.
(22) Milošević, D. B.; Paulus, G. G.; Bauer, D.; Becker, W. *J. Phys. B: At. Mol. Opt. Phys.* **2006**, *39*, R203.
(23) Becker, W.; Grasbon, F.; Kopold, R.; Milošević, D. B.; Paulus, G. G.; Walther, H. In *Advances In Atomic, Molecular, and Optical Physics*; Elsevier: New York, 2002; Vol. *48*, pp 35−98.
(24) Paulus, G. G.; Becker, W.; Walther, H. *Phys. Rev. A* **1995**, *52*, 4043−4053.
(25) Passlack, S.; Mathias, S.; Andreyev, O.; Mittnacht, D.; Aeschlimann, M.; Bauer, M. *J. Appl. Phys.* **2006**, *100*, 024912.
(26) Siwick, B. J.; Dwyer, J. R.; Jordan, R. E.; Miller, R. J. D. *J. Appl. Phys.* **2002**, *92*, 1643−1648.
(27) Arafune, R.; Hayashi, K.; Ueda, S.; Ushioda, S. *Phys. Rev. Lett.* **2004**, *92*, 247601.
(28) Zhou, X. J.; Wannberg, B.; Yang, W. L.; Brouet, V.; Sun, Z.; Douglas, J. F.; Dessau, D.; Hussain, Z.; Shen, Z.-X. *J. Electron Spectrosc. Relat. Phenom.* **2005**, *142*, 27−38.
(29) Schenk, M.; Krüger, M.; Hommelhoff, P. *Phys. Rev. Lett.* **2010**, *105*, 257601.
(30) Valfells, Á.; Feldman, D. W.; Virgo, M.; O'Shea, P. G.; Lau, Y. Y. *Phys. Plasmas 1994-Present* **2002**, *9*, 2377−2382.
(31) Ding, M.; Sha, G.; Akinwande, A. I. *IEEE Trans. Electron Devices* **2002**, *49*, 2333−2342.